STATE RESEARCH CENTER OF RUSSIA

INSTITUTE FOR HIGH ENERGY PHYSICS

REPORT

Preliminary Design Work and Neutrino Beam Calculations for the NuMI Project

(Tasks A and B of the Accord between FNAL and IHEP)

A.Abramov, I.Azhgirey, P.Galkin, N.Galyaev, V.Garkusha,
A.Kharlamov, Yu.Khodyrev, S.Knyazev, I.Kurochkin, E.Lomakin,
F.Novoskoltsev, A.Ryabov, V.Seleznev, Z.Sharifullin, E.Ustinov,
V.Zapolsky, V.Zarucheisky

Protvino 1997

Contents

1 Short Summary of the Target Design

At this stage of the target station design the main attention was paid to optimization of parameters of the target heads and to the choice of cooling means. Besides, the design principles and possible technical solutions were investigated for the target assembly, the device for correct installation of the target on its position, beam detectors, alignment mechanisms, means of target replacement from the "hot zone", and other components. The layout of the target station, including the surrounding shielding and upstream and downstream nearby equipments, was also being adjusted.

In order to find the optimal material, configuration, and cooling of the target heads, the computations were carried out studying the deposited energy distributions, temperature fields, and secondary particle production. The basic configurations of the target heads (cylinder, plate, and fin) are shown in Figure 1.1. At the moments the most complete calculations have been carried out for cylindrical targets. Some results are given below.

1.1 Energy Deposition

Computer programs MARS (for example, [1]) were used to compute the energy distribution deposited by the primary proton beam in the targets.

It was assumed that the primary proton beam energy was 120 GeV, the intensity $4{\cdot}10^{13}$ ppp, and the Gaussian intensity distribution had equal RMS values in the horizontal and vertical planes ($\sigma_x{=}\sigma_y{=}\sigma_p$). In these calculations the proton beam RMS size varied within 0.03–0.2 cm. Beryllium, graphite, and nickel as material for the target heads were taken. For all the listed materials the dependence of the maximum deposited energy density Q_{max} (GeV/g/proton) on the proton beam size is shown in Figure 1.2. Here Q_{max} is the average value for cells with the radius r = $0.5{\cdot}\sigma_p$ coaxial to the target axis and the length step Δz = 20 cm in the region of maximum deposited energy. For beryllium and graphite, Figure 1.3 presents the maximum temperature rise ΔT_{max} as a function of the beam size. The temperatures ΔT_{max} have been calculated in the assumption of adiabatic heating (pessimistic estimation).

Histograms in Figures 1.4, 1.5, and 1.6, for beryllium, graphite and nickel correspondingly, show the longitudinal dependence of the deposited energy density Q_0 along the target axis upon the proton path length z in

the target for various sizes of the proton beam. The points in Figures 1.4 and 1.5 give Q_0 for the 10–segment targets at the proton beam size of $\sigma_p = 0.07$ cm. The length of each segment is equal to 10 cm, radius is equal to 0.2 cm. The segments are separated by 10 cm gaps.

For graphite targets with radii of 0.1, 0.2, and 0.5 cm and the beam size of $\sigma_p = 0.07$ cm, Figure 1.7 presents the linear density of the deposited energy Q_{lin} (radius-integrated energy density for Δz length of 10 cm). The points also correspond to the segment target as described above.

For beryllium and graphite targets with lengths of 100 cm, the total deposited energy Q_{tot} (in GeV/100 cm per 1 proton and kJ/100 cm per $4{\cdot}10^{13}$ protons) is shown as a function of the target radius in Figure 1.8. In the case of the segment target the energy Q_{tot} is smaller by approximately 30%.

1.2 Temperature and Cooling

Estimations of the efficiency of various means for the target cooling were made: a forced gas convection plus radiation and heat conductivity plus a forced water cooling.

In the case of helium cooling of the cylindrical graphite target with radius of 0.2 cm, the steady–state temperatures were calculated at the flow velocities of 4, 10, and 20 m/s for the maximum energy–deposition zone. The temperatures were equal to 800, 510, and 360 ^{0}C, correspondingly. As shown earlier for the plate and fin targets without grooves and with the thickness of 0.4 cm, the steady–state temperatures were within 100–200 ^{0}C (the low value is for plate, and the upper one is for fin). For the plate/fin targets with grooves of 0.2 cm and with thickness of 0.4 cm in the proton beam region (see Figure 1.1 b and c) the steady-state temperatures were equal to 150–300 ^{0}C for graphite target and to 100–200 ^{0}C for beryllium target. To reduce the temperature, several cooling means must be applied. Detailed computations of the temperatures and thermal stresses are in progress.

1.3 Production Efficiency and Configuration

To study the target efficiency, the pion flux emerging from the target in the definite intervals of energy and angles was calculated for various con-

figurations of the target head. For graphite target of the length of 100 cm, Figure 1.9 shows the character of the pion yield as a function of the target radius at different sizes of the proton beam. Figure 1.10 gives the ratio of R_{opt} to the beam size and of the pion yield as functions of the beam size.

The influence of the longitudinal configuration on the target efficiency was considered for the segment target. For the pion flux calculation for a wide–band neutrino beam, the secondary beam optics, using parabolic lenses, was taken into account. The relative efficiencies of the following configurations for the graphite target with $R_t = 0.2$ cm and the proton beam RMS size of 0.07 cm are given below:

- lengthened uniform target with the material density of 1.16 g/cm^3, $L = 156$ cm, 100.0%;
- 3–segment target with segment lengths of 20, 20, and 60 cm and with 16 cm gaps, $L = 132$ cm, 99.6%;
- 2–segment target with segment lengths of 50 and 50 cm and with 20 cm gap, $L = 120$ cm, 96.8%;
- 8–segment target with each segment length of 12.5 cm and with 8 cm gaps, $L = 156$ cm, 95.0%;
- uniform target with the material density of 1.81 g/cm^3, $L = 156$ cm, 86.0%.

In the case of the secondary beam optics using parabolic lenses for narrow–band neutrino beam, it is obtained that beryllium and graphite targets are more effective in comparison with nickel target.

1.4 Layout and Alignment

Figure 1.11 gives the vertical longitudinal cut of the target station, showing the principal layout. In this layout the station element support and all active components such as the displacement mechanisms, the motors, the control equipments, the instrumentation and the connections are mounted on the top of the shielding.

In Figures 1.12 and 1.13 the design of the target unit–alignment platform ensemble is presented. The alignment platform provides the horizontal and vertical displacement of the target unit as well as the change of its horizontal and vertical angles to the beam axis. The basic components of the alignment platform assembly are:

- primary frame with jacks for manual alignment;
- guides of horizontal and vertical movements;
- servomechanisms with electrical motors of direct current;
- two channel system of coordinate (rough and fine channels) and switch status determinations;
- position calibrating device mounted in a "hot zone";
- rigid suspension shafts.

The following parameters for the alignment platform have been assumed:

Horizontal and vertical displacement limits, mm	± 20
Movement velosity, mm/s	5
Turning angle limits in both planes, mrad	± 2
Angular velocity, mrad/s	1
Electrical power supply:	
voltage, V	220
frequency, Hz	50-60
Electrical power comsumption, kW	10
Mass, kg	500

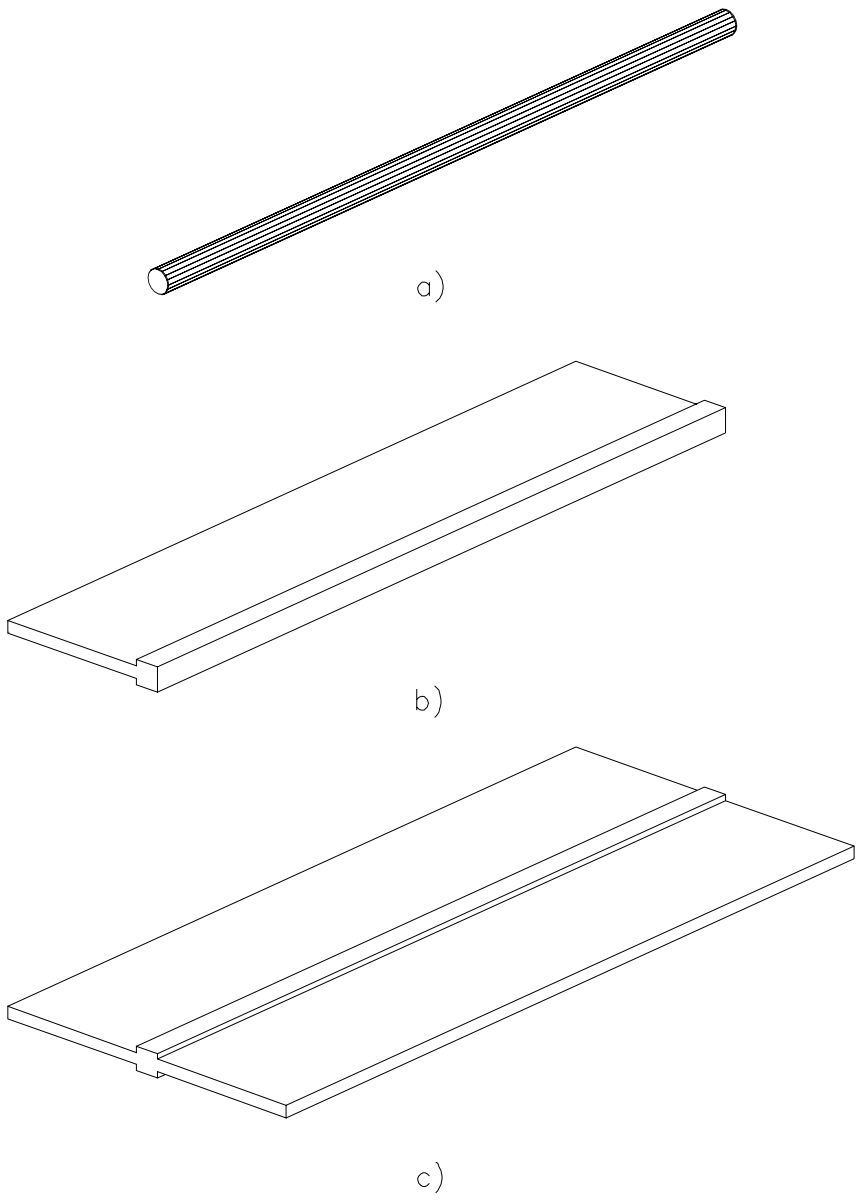

Figure 1.1: Configuration of the target heads.

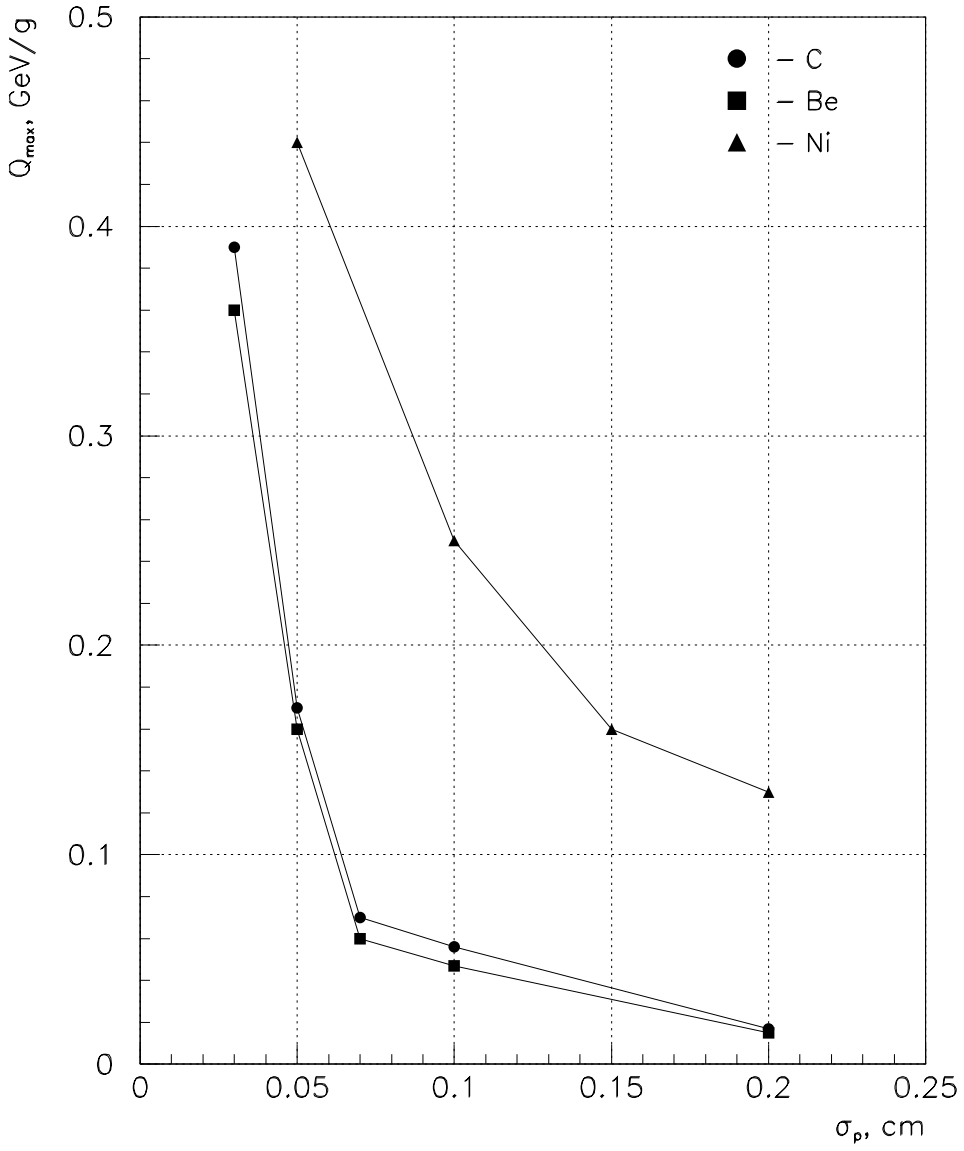

Figure 1.2: The maximum energy density deposited per proton as a function of the proton beam RMS size.

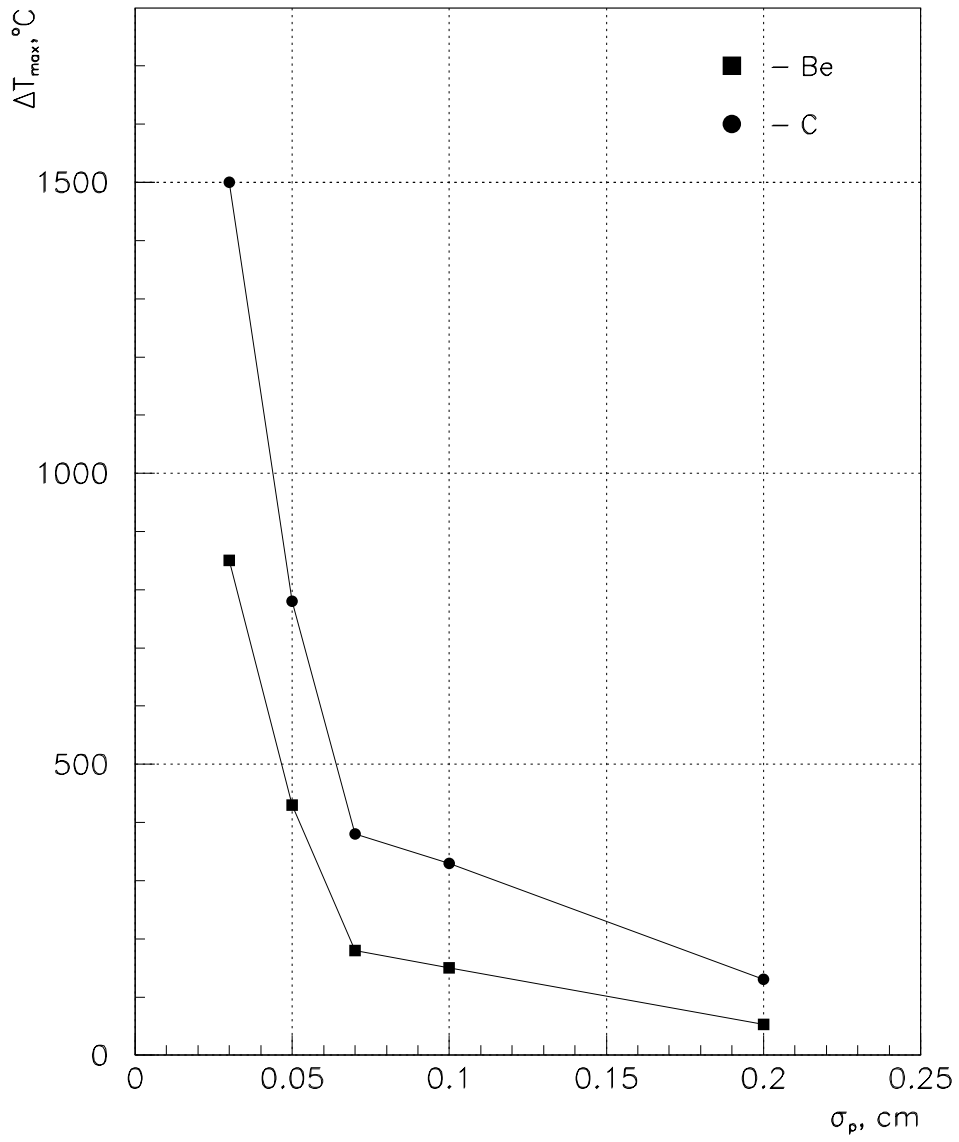

Figure 1.3: The maximum temperature rises at the adiabatic heating for Be and C targets versus the proton beam RMS size.

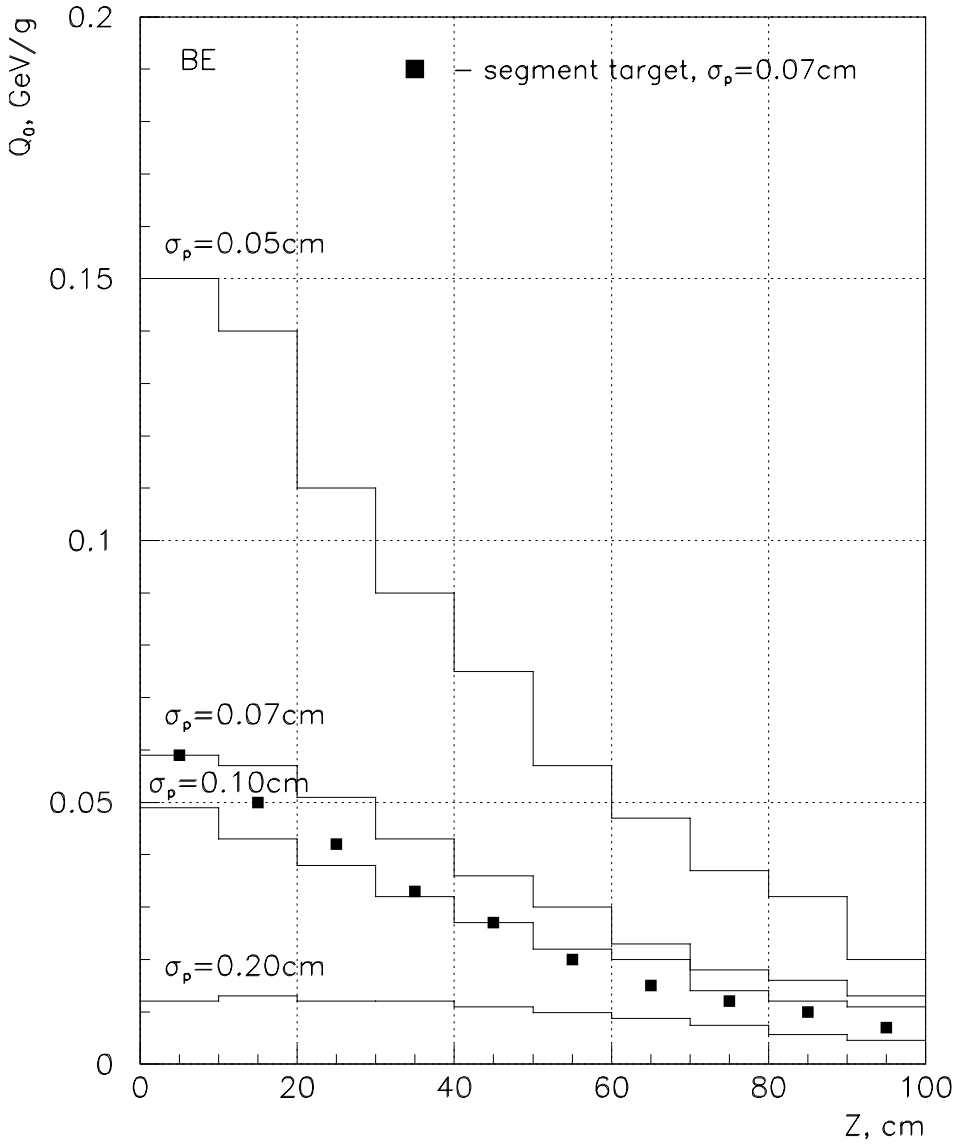

Figure 1.4: The longitudinal distributions of the deposited energy density along the beryllium target axis.

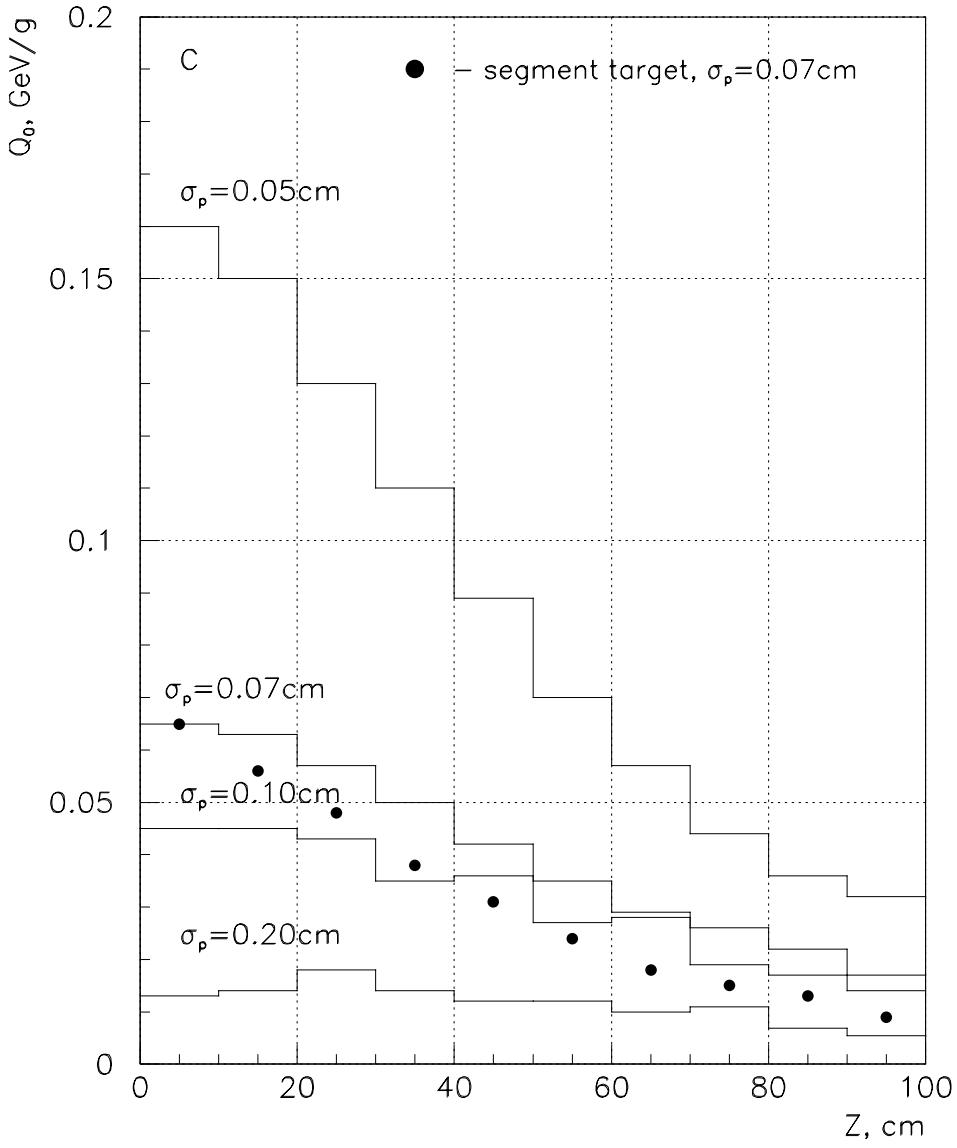

Figure 1.5: The longitudinal distributions of the deposited energy density along the graphite target axis.

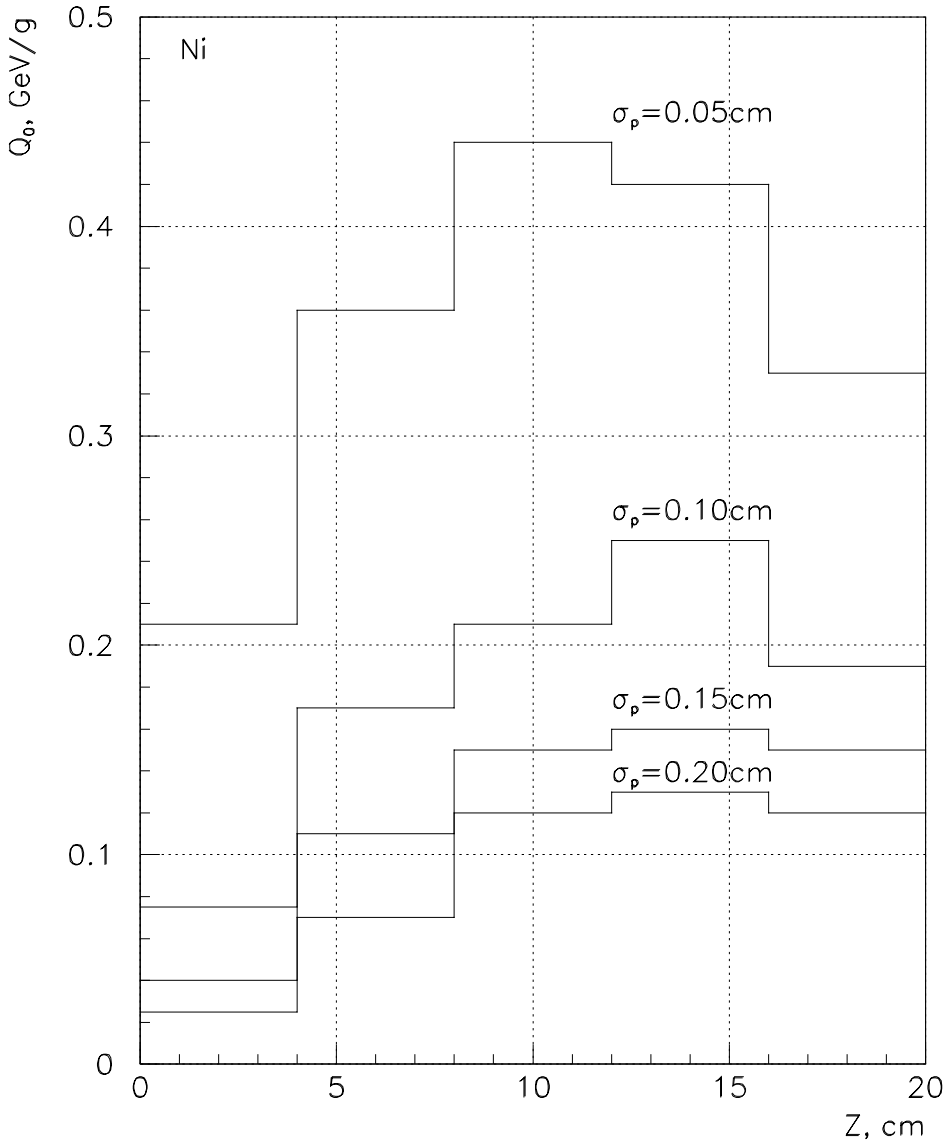

Figure 1.6: The longitudinal distributions of the deposited energy density along the nickel target axis.

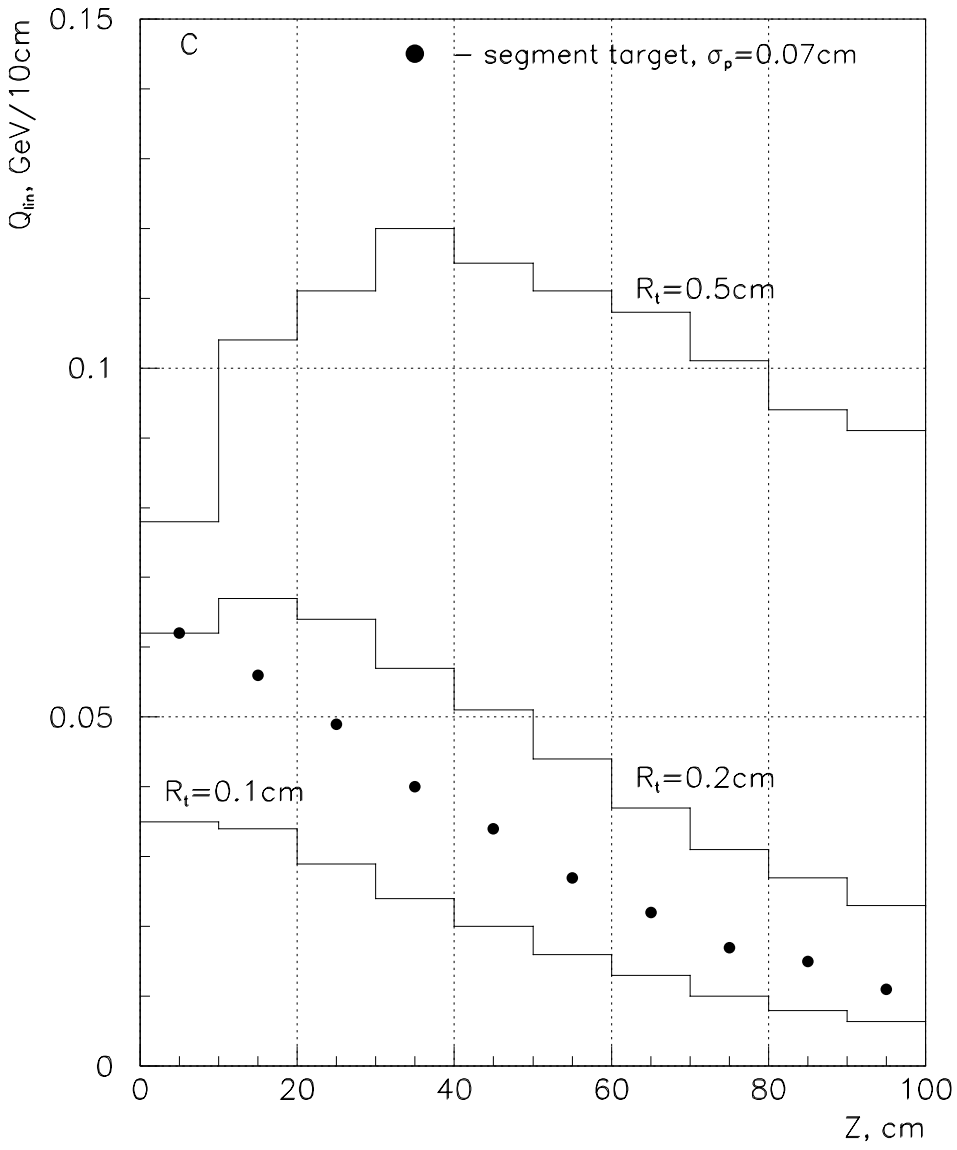

Figure 1.7: The longitudinal distributions of the linear of the energy dissipation at different radii of the graphite target.

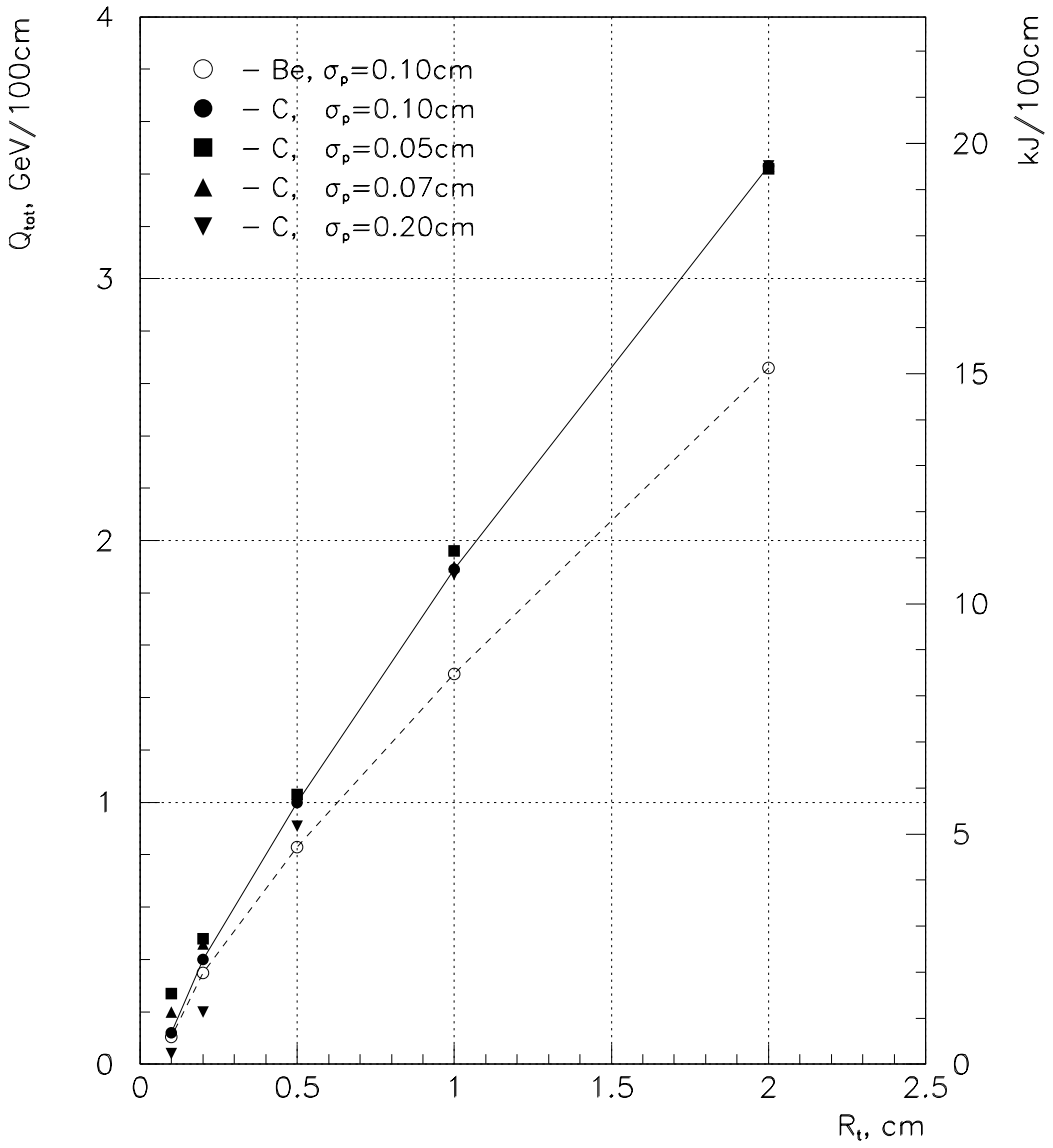

Figure 1.8: The total energy dissipation for the beryllium and graphite targets of 100 cm length as a function of the target radius for different proton beam RMS size.

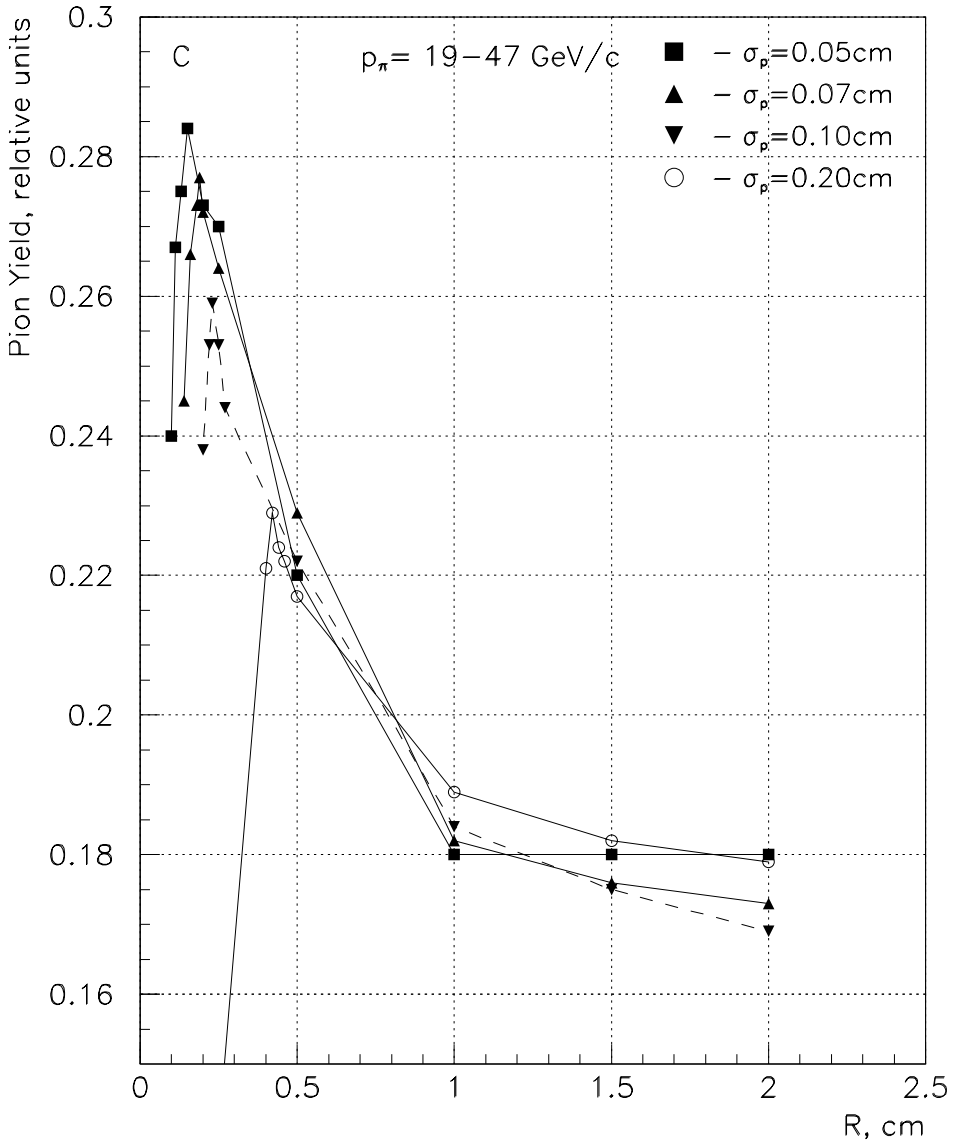

Figure 1.9: The pion yield for the graphite target at different proton beam RMS size versus the target radius.

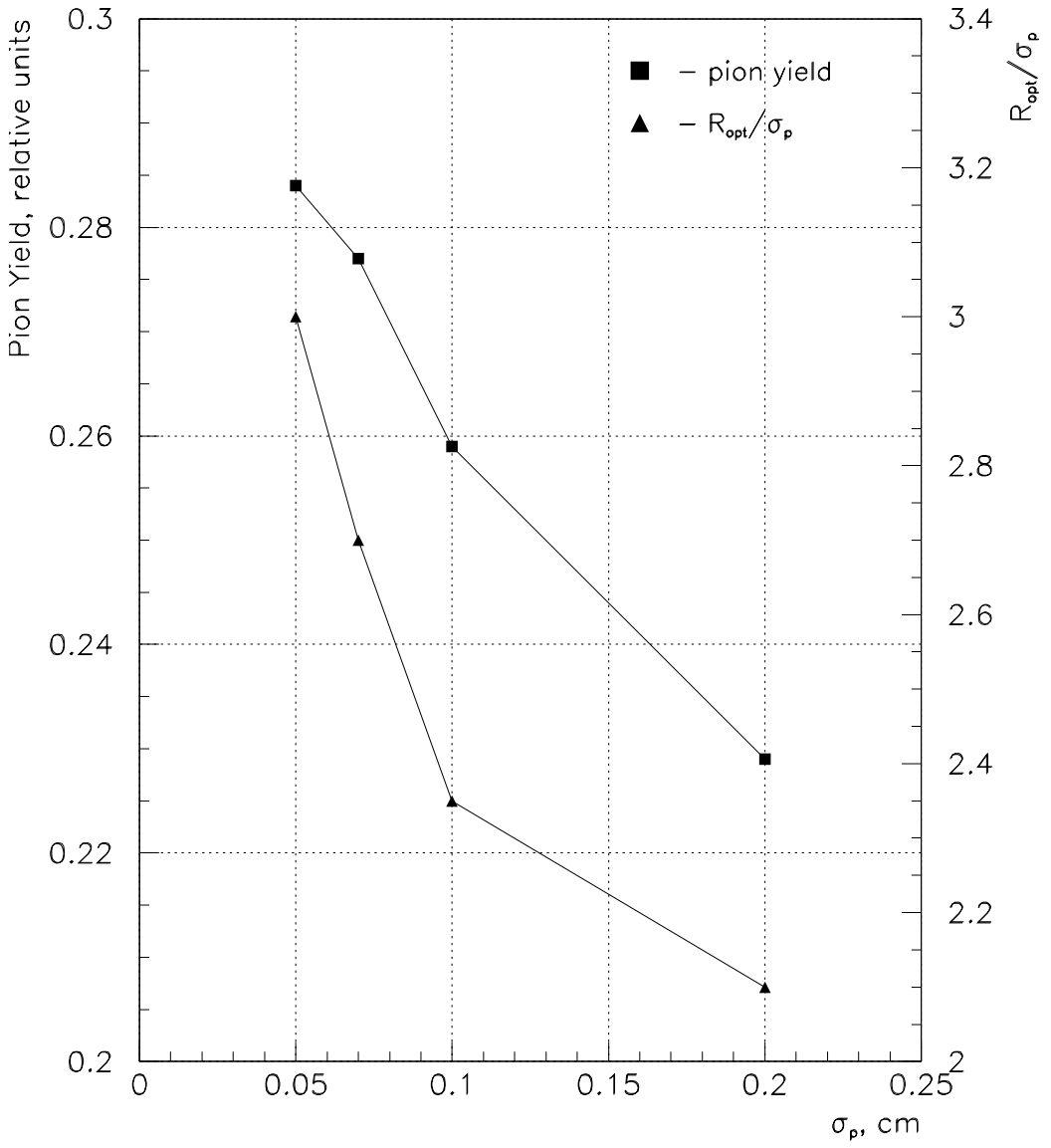

Figure 1.10: The ratio of R_{opt} to proton beam RMS size and pion yield at the target radius R_{opt} as functions of the proton beam RMS size.

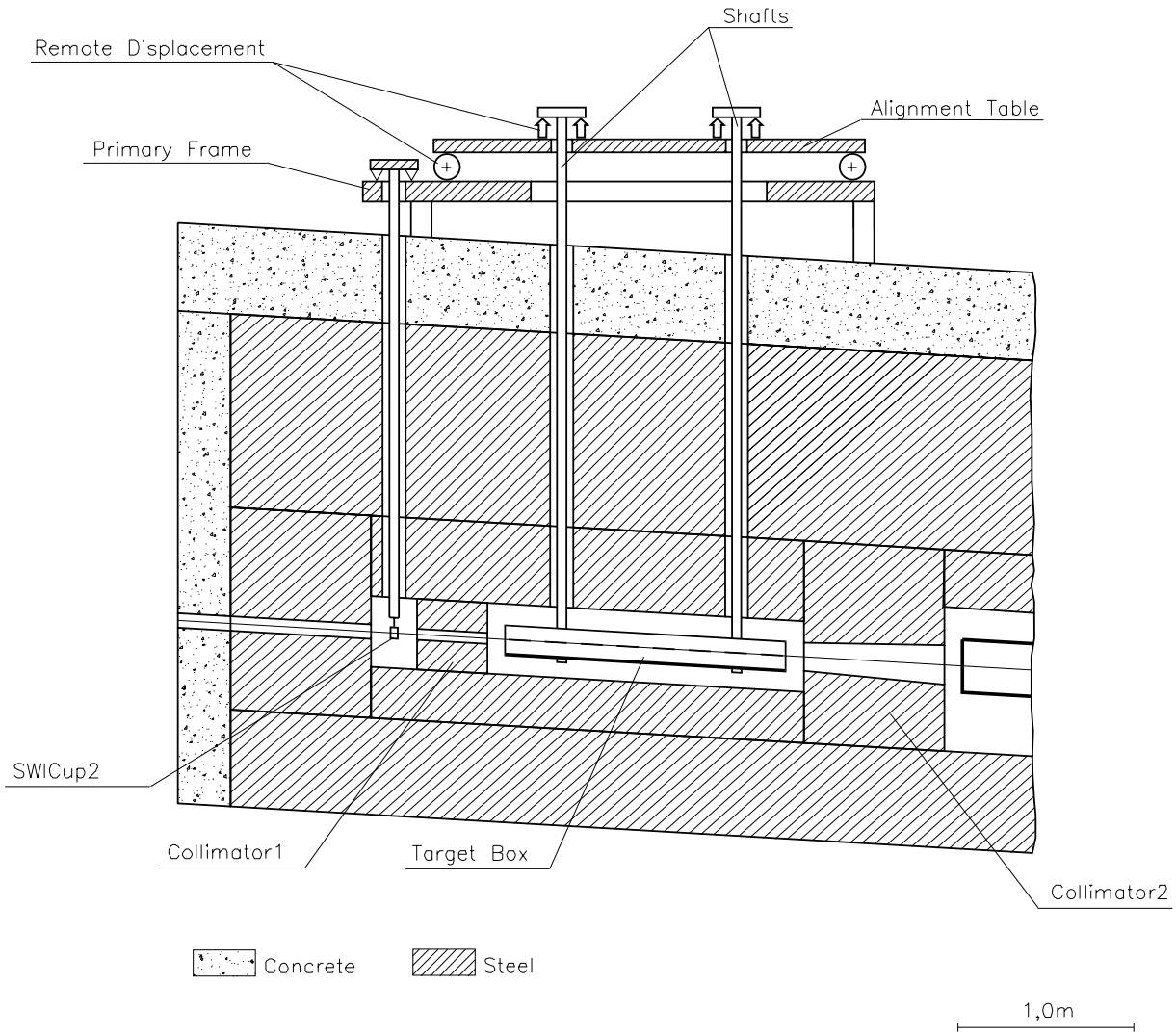

Figure 1.11: The vertical cross-section of the target station.

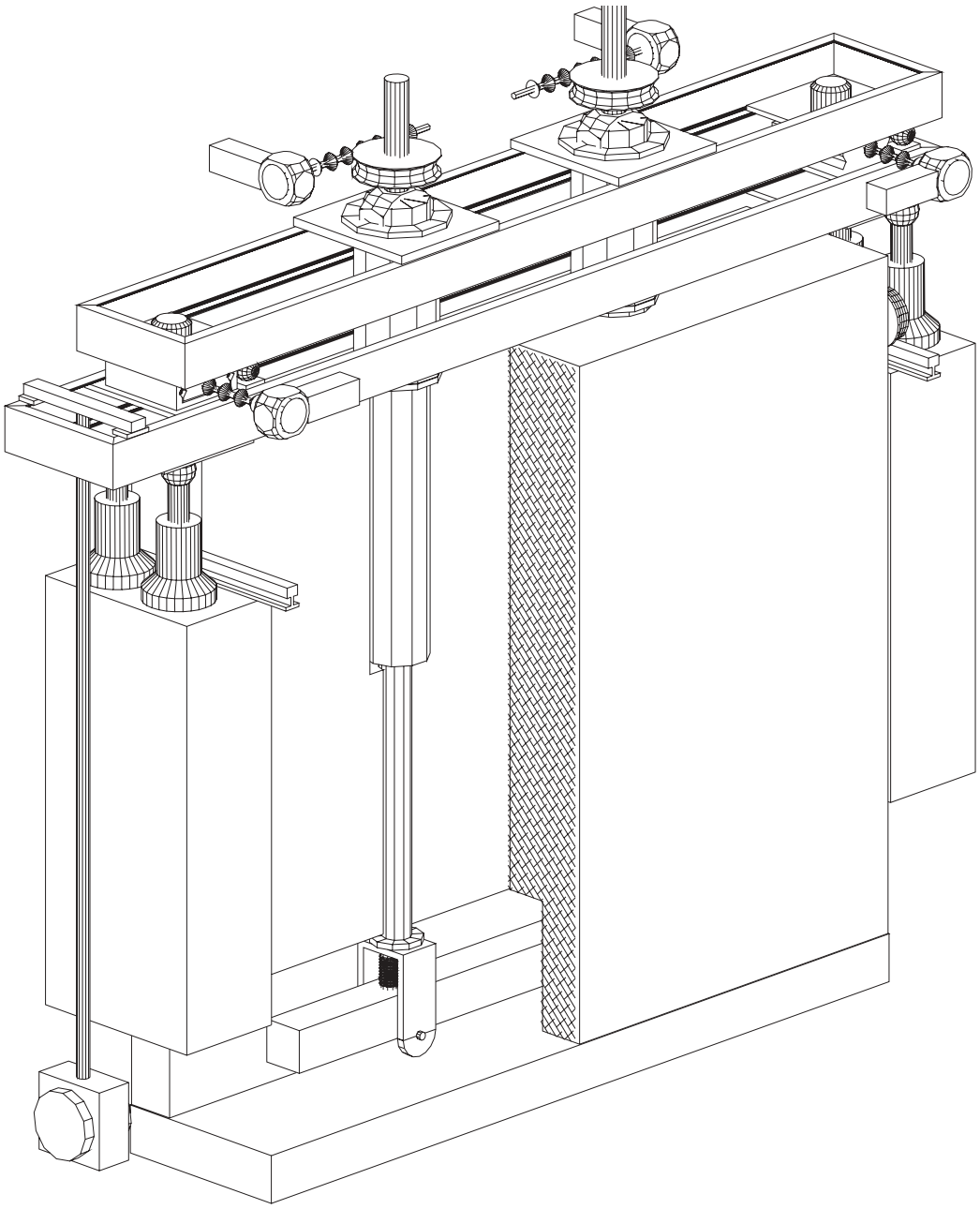

Figure 1.12: The layout of the target unit-alignment platform.

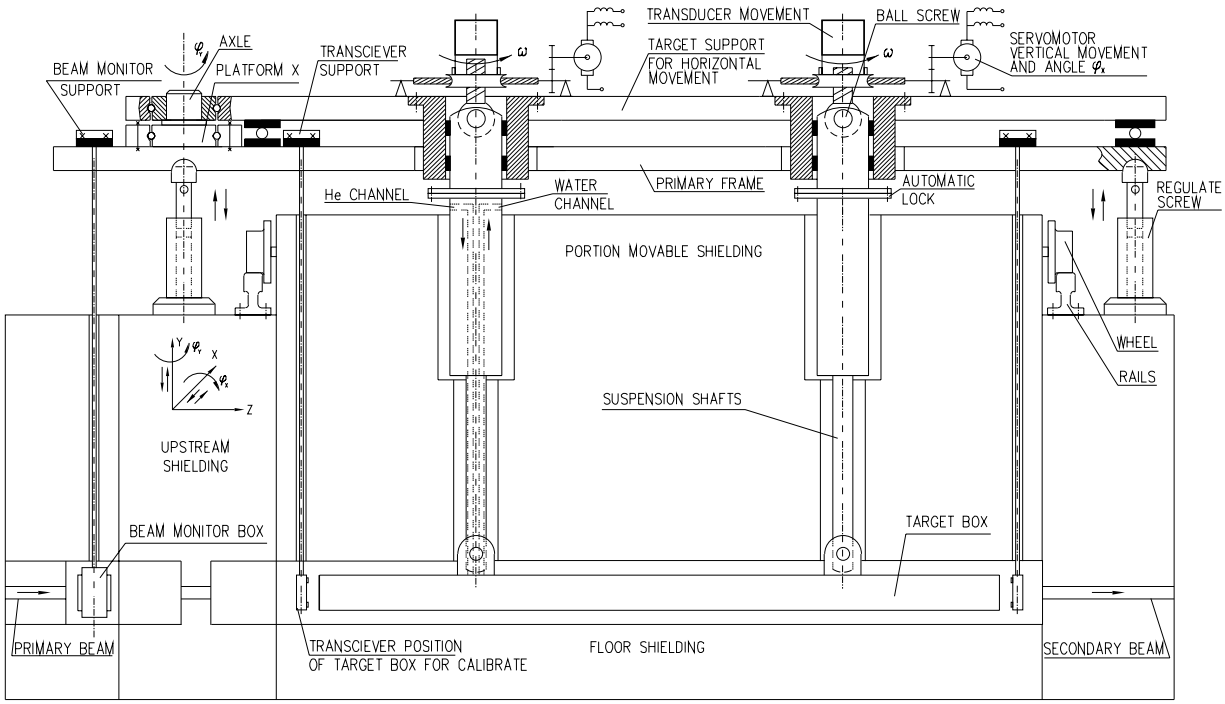

Figure 1.13: The design of the alignment platform.

2 NuMI Neutrino Beams using the Parabolic Horn (Lens) Focusing System

A focusing system with parabolic lenses has been elaborated and produced at IHEP for the 70 GeV wide band neutrino beam [2]. The inner conductor of a parabolic lens consists of two paraboloids connected together at their tops by a small neck with a hole inside. The inner conductors were casted from aluminium alloy and afterwards machined to the needed dimensions. All lenses have been developed for the 500 kA with 160 μs current pulse and the machine cycle of 8.8 sec. To provide maximum neutrino flux with minimal background from the parents of an opposite sign, the focusing properties of multi–lens systems have been studied in detail. An overall reliability of this system is confirmed by the 15 years successful operation.

As a possible focusing system for the neutrino beams of the NuMI project we have studied the focusing systems with parabolic lenses. The main geometrical dimensions of parabolic lenses, which have been used to design the focusing system for both WBB and NBB, are given in Table 2.1.

Lens No.	Parabola parameter,cm^{-1}	Full length of lens,cm	Max. radius,cm	Neck radius,cm	Hole radius,cm
L1	0.824	74	6.4	1.2	0.4
L2	1.000	128	8.0	1.7	0.8
L3	0.124	143	24.0	3.0	1.5

Table 2.1: Geometrical dimensions of parabolic lenses.

2.1 Wide Band Neutrino Beam

A focusing system with three L1 and two L3 lenses (3L1/2L3) has been investigated for the WBB. A schematic layout for this focusing system is shown in Figure 2.1. The currents in both sets of lenses are equal to 320 kA.

The spectrum and total event rate at the far detector compared with those for a three horn focusing system H6.6 are shown in Figure 2.2. The two nuclear interaction length target described in NuMI Technical Design Report [3] was used for both optics designs. Calculations of neutrino fluxes shown above have been made using the Fermilab program NUADA [4].

Besides NUADA, a Monte Carlo program HALO was used for neutrino flux (events) calculations. This program originally written in CERN [5] has been modified to produce a weighted neutrino in the detector acceptance. Absorption and scattering of hadrons in the horn walls are taken into account, but secondary particles are not generated. Each hadron is decayed at each step along its track. HALO allows to track hadrons through thick horn walls more accurately than NUADA, what is important for the neutrino flux calculations in the case of parabolic horns focusing system. This version of HALO allows to take into account the real target size and proton beam distribution at the target.

Figure 2.3 shows the neutrino spectra at the far detector for both H6.6 and 3L1/2L3 focusing systems calculated using program HALO for two nuclear interaction length target with radius 0.2 cm and proton beam RMS size 0.1 cm. As follows from this Figure, the parabolic lens focusing system 3L1/2L3 has smaller event rate by about 9% with respect to the three horn design H6.6.

It follows from our preliminary results, that usage of two lenses L2 instead of three lens L1 (2L2/2L3 focusing system) gives some reduction in the total event rate at the far detector. But relatively thick walls of the casting for the lens L2 permits to fabricate from this casting the lens with few different parameters as compared to originally planned. This new lens LX may be used to create the focusing system 2LX/2L3. Preliminary, this new lens LX will have some positive properties with respect to lens L1 from the point of view of technical design (temperature, stresses, assembly). The parameters of LX will be optimized at the next stage.

The spectrum and total event rate at the far detector for the focusing system 2LX/2L3 compared with those for 3L1/2L3 focusing system are shown in Figure 2.4. The total event rate for 2LX/2L3 focusing system is only 2% smaller than that for H6.6 WBB one.

2.2 Narrow Band Neutrino Beam

The parabolic lenses can be also used for creation of the NBB focusing system [6]. Figure 2.5 shows the a schematic layout for 3L1/2B/2L3 focusing system, which provides the neutrino beams for hadron beam energies from 20 to 45 GeV. Three dipoles (one before the target) and collimator are added to the 3L1/2L3 WBB optics to select $\Delta p/p$ in the secondary beam

and to dump the primary protons. This optics allows to have a simple change between WBB and NBB designs, in particular one may exclude any displacements on the primary proton beam-line. The maximum separation between WBB and NBB axes is equal to 0.2 m.

The tuning to various momenta can be done by changing the currents in parabolic lenses and dipoles, while keeping the target and all equipment at fixed positions. The currents in parabolic lenses (I_1/I_2) are equal to 320/320 kA for 20 and 45 GeV tunes and 320/190 kA for 30 GeV tune. Because of a relatively large depth of the field in the parabolic lens focusing system, as compared to lithium lens design, it permits the use of low-density (C or Be) targets.

The spectra and the total muon neutrino event rate at the far detector calculated by HALO for two different targets are plotted in Figure 2.6 for the proposed 3L1/2B/2L3 focusing system. The radius of each target is equal to 0.2 cm and the proton beam RMS size is equal to 0.1 cm. A two nuclear interaction length WBB (long) target gives an increase in the total event rate with respect to one interaction length (short) target by a factor of 1.15–1.40 for 20–45 GeV tunes respectively, while the RMS size of neutrino energy spectra remains just the same as for the short target. One should note that new lens LX can be also used to create the NBB focusing system 2LX/2B/2L3. This system allows to obtain the neutrino parameters at the far detector, which are better than one for the 3L1/2B/2L3 focusing system.

One of the design goals for the NBB is to minimize the low energy tail of the beam energy spectrum. Significant part of the low energy neutrino is going from secondary interactions in the collimators walls and the horns, which are beyond the HALO capabilities. The Fermilab beam simulation package GNUMI has been used in order to obtain correct results for the low energy tail of neutrino beam in the proposed NBB design with parabolic lens.

Figure 2.7 shows the energy spectra for the 3L1/2B/2L3 focusing system with two different targets at 45 GeV tune. As follows from these beam simulations, the ratio of the neutrino events with $E < 10$ GeV to the total number of neutrino events is equal to 0.6% for both targets, while the total event rate goes from 606 to 848.

WBB. 3*L1/2*L3 Focusing System.

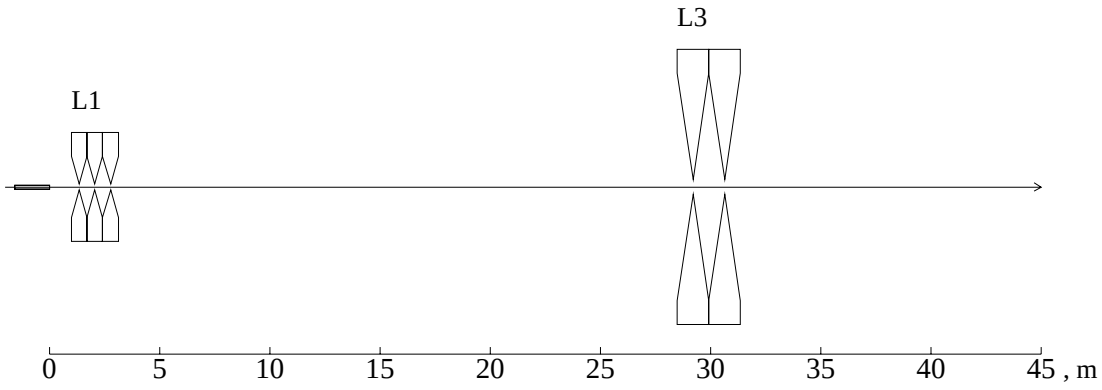

Figure 2.1: The layout of a 3L1/2L3 focusing system for the WBB.

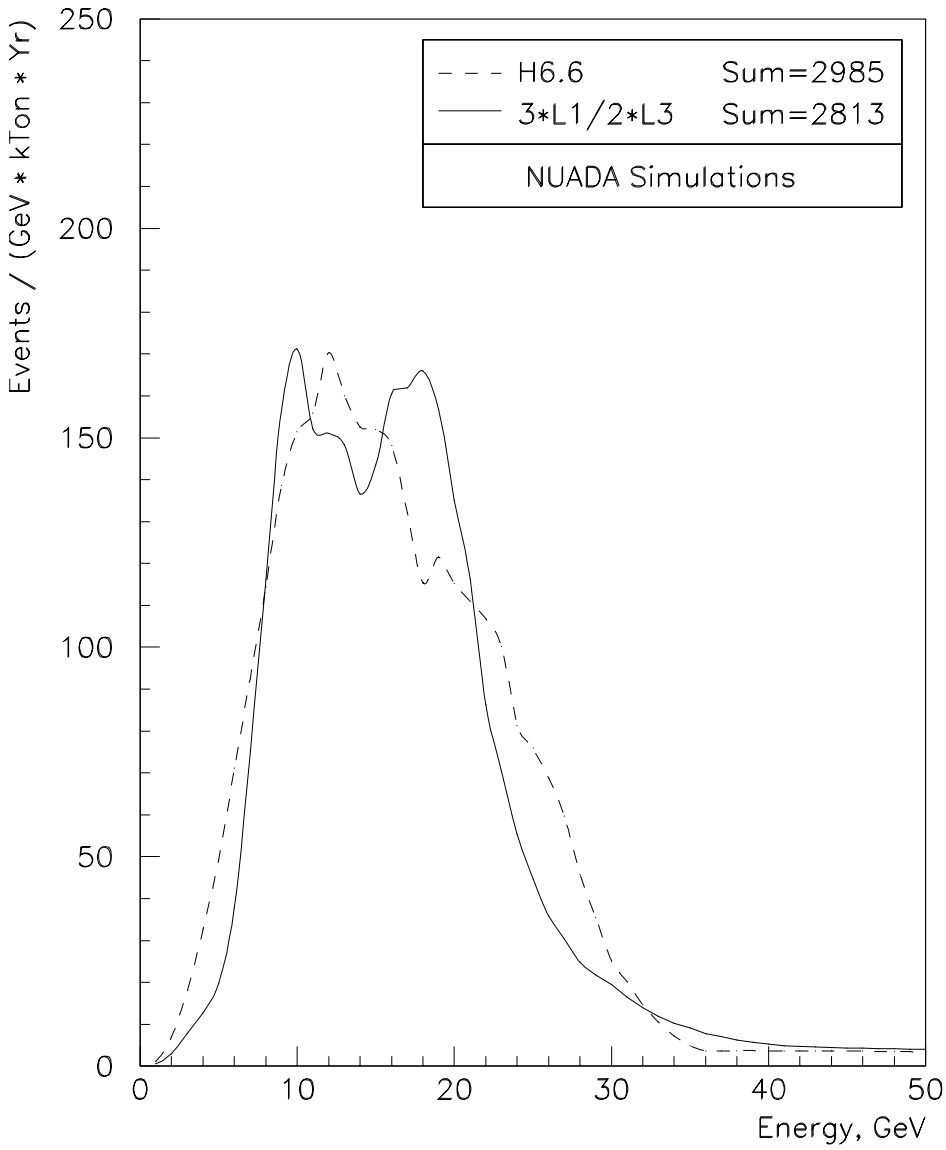

Figure 2.2: ν_μ event rate for a H6.6 and 3L1/2L3 focusing systems.

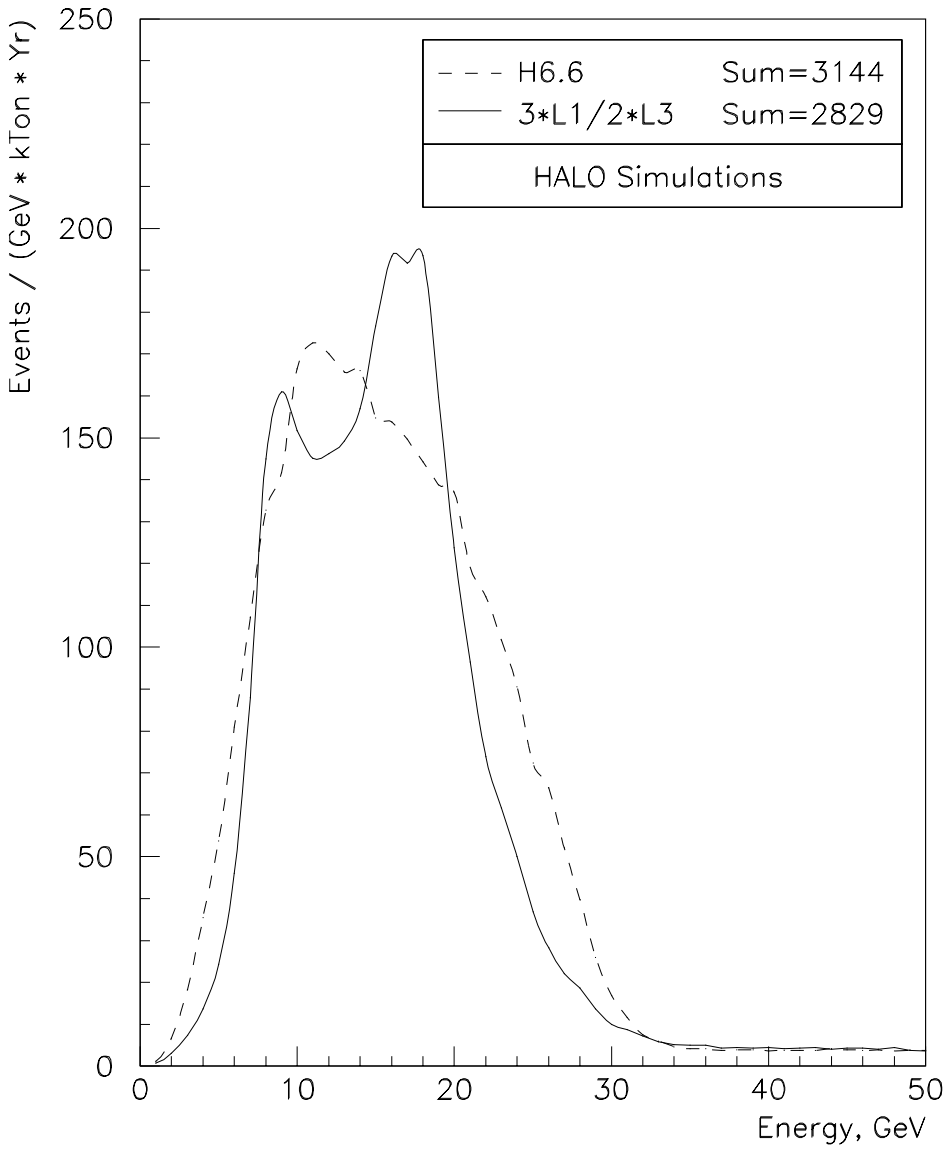

Figure 2.3: ν_μ event rate for a H6.6 and 3L1/2L3 focusing systems.

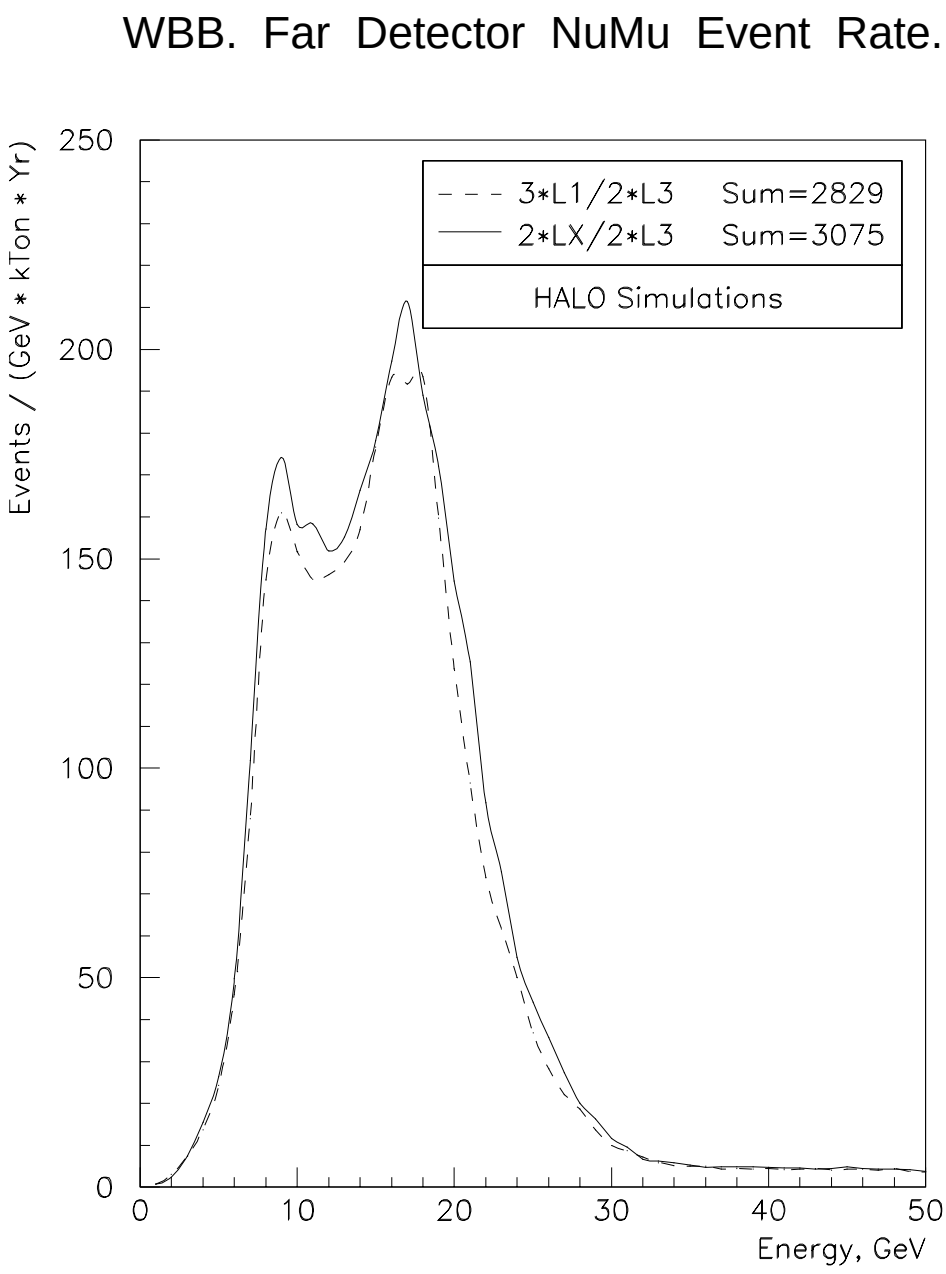

Figure 2.4: ν_μ event rate for a 3L1/2L3 and 2LX/2L3 focusing systems.

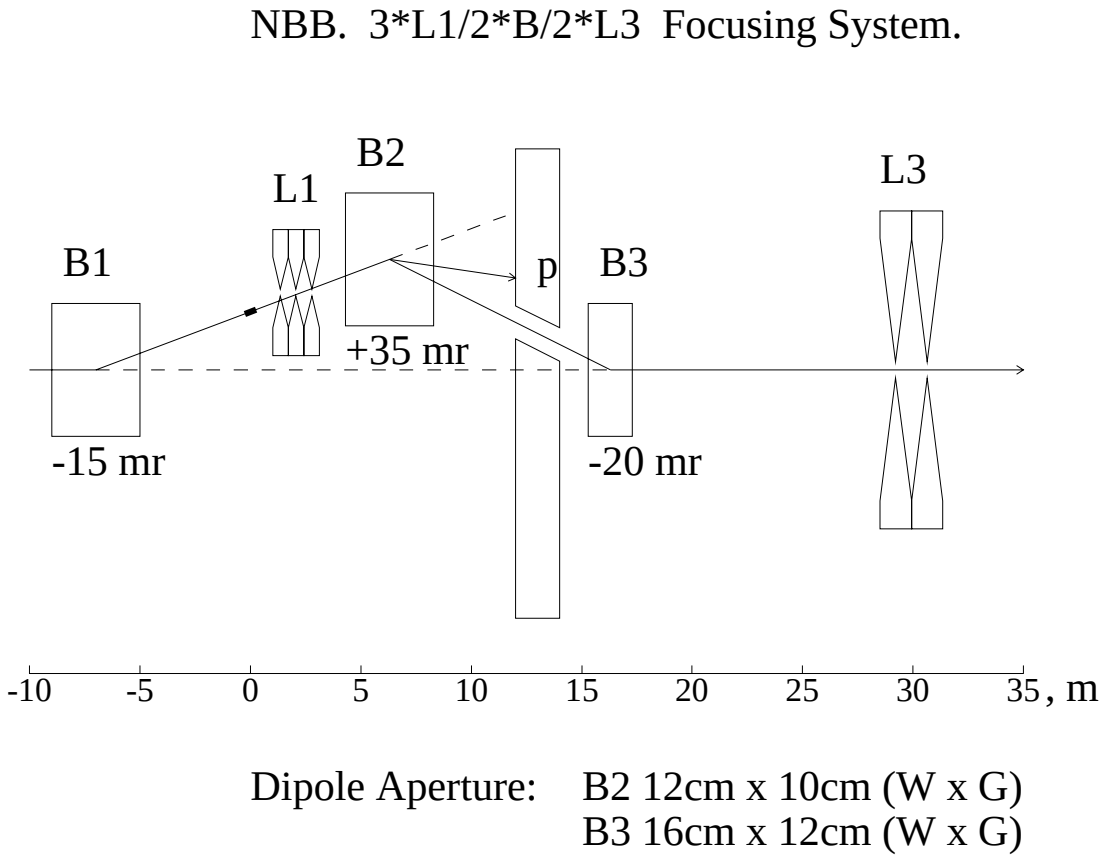

Figure 2.5: The layout of a 3L1/2B/2L3 focusing system for the NBB.

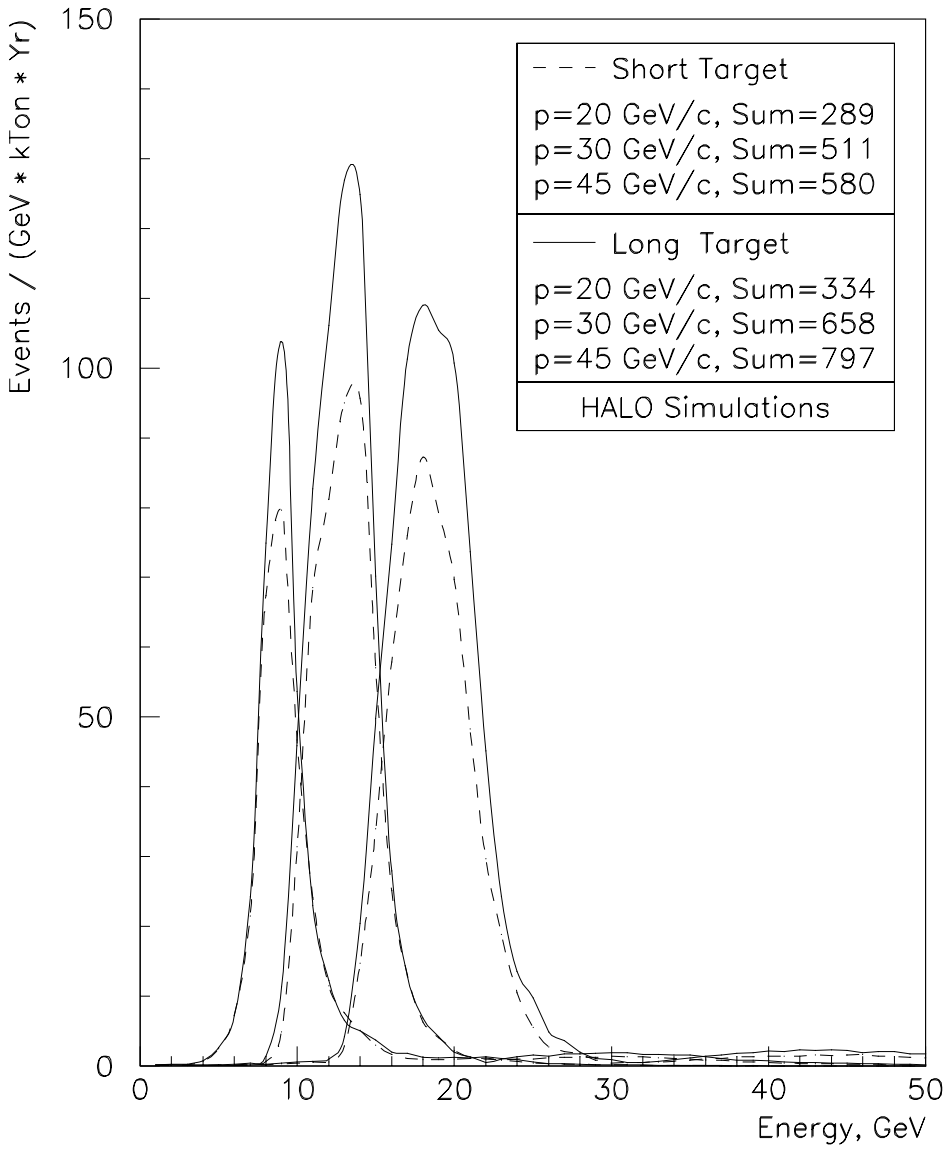

Figure 2.6: ν_μ event rate for a 3L1/2B/2L3 focusing system.

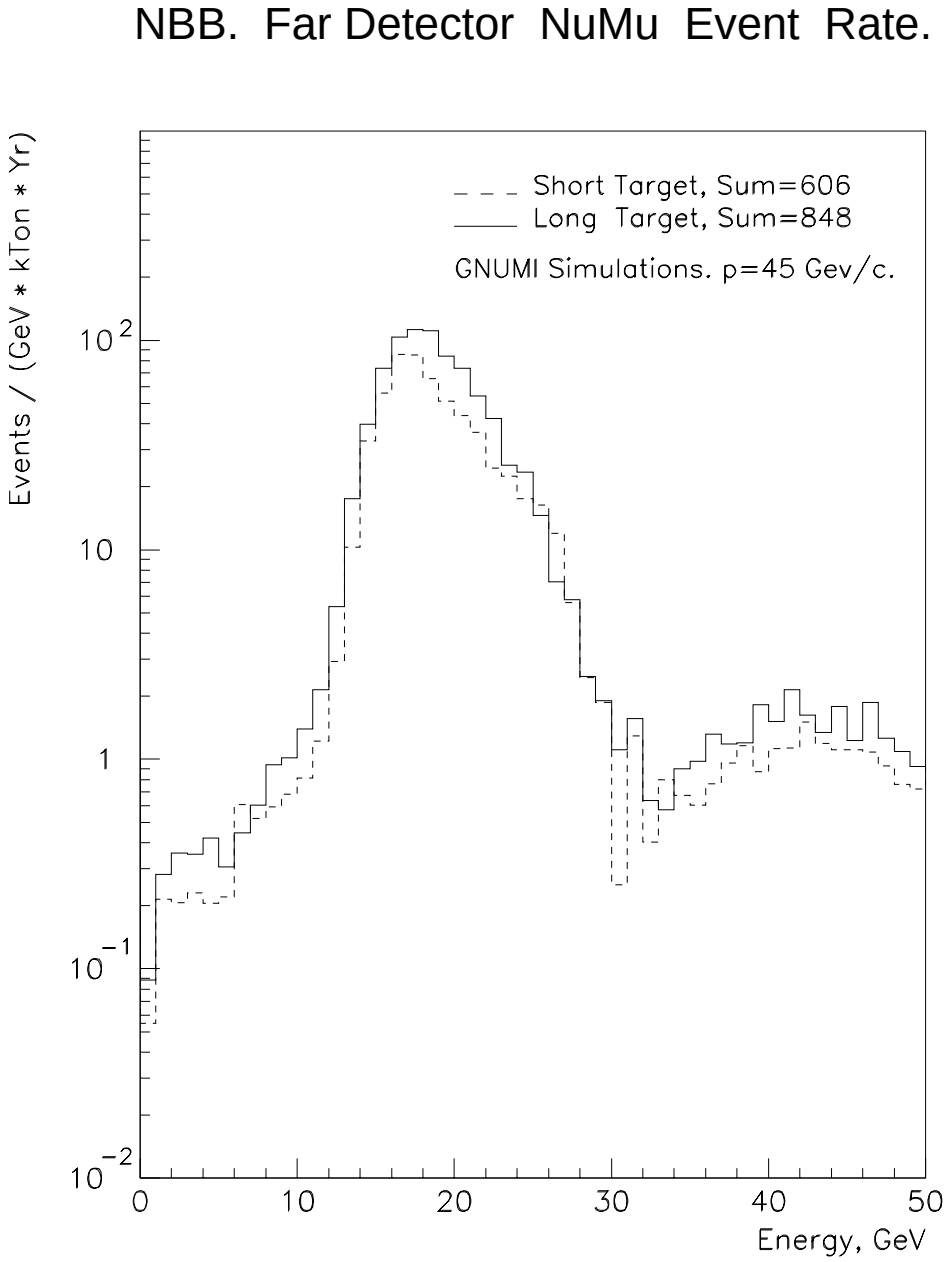

Figure 2.7: ν_μ event rate for a 3L1/2B/2L3 focusing system.

3 Parabolic Lenses

3.1 Lens Parameters

The parabolic lens design consists of two cylindrically symmetric current shells. The inner conductor is described by $r = \sqrt{(z-h)/p}$, where r is the radius, p the parabola parameter, z the length, h the parabola shift. For outer surface $h = 0$, for inner surface of parabolic shell $h \neq 0$. The outer conductor is cylindrical with wall thickness of 1 cm. The geometrical dimensions of the parabolic lenses existing at IHEP are given in Table 2.1.

Lenses L1 and L3 are machined out of the castings of Al-alloy B2243 produced by the "MOLNIYA" plant, Moscow. Table 3.1 lists the properties of this material.

Density d, kg/m^3	2.77×10^3
Specific heat c_p, J/(kg·K)	900
Coefficient of thermal expansion α, 1/K	22.3×10^{-6}
Thermal conductivity λ, W/(m·K)	149
Modulus of elasticity E, N/mm^2	6.965×10^4
Static yielding stress σ_t, N/mm^2	323
Dynamic fatigue stress limit, N/mm^2 @ cycles	98.1 @ 2.0×10^7
Resistivity ρ, Ohm·cm	5.46×10^{-6}

Table 3.1: Properties of Al - alloy B2243.

Lens L2 exists only as a casting but of another Al – alloy B2243-8. It has the properties as listed in Table 3.1, but the mechanical properties are 1.36 times higher.

Both focusing devices, 3L1 and 2L3, are the assemblies of few lenses bolted together: the first one consists of 3 lenses L1 and the second one — of 2 lenses L3. The thickness of connecting flanges is equal to 1 cm. The dielectric (ceramic) supports between the connecting flanges and the outer conductor are provided in order to prevent the sagging of inner conductor and to damp its transverse vibration, but to allow the inner conductor to move longitudinally. The cooling of the inner conductor is produced by a low conductivity water sprayed from the system of external pipes through the holes in the outer conductor.

Computed electrical parameters of focusing devices are listed in Table 3.2. The duty factor Q was calculated assuming that

$$I(t) \sim \exp(-\alpha t) \sin\left(\frac{2\pi t}{T}\right),$$

where T= 10 msec, α is defined by the focusing device parameters L, R and inductance L_s and resistance R_s of the 10 m strip–line.

Parameter	Focusing device 1	Focusing device 2
Inductance L, nH	318	327
Resistance R, μOhm	217	69
Peak current I, kA	320	320
Duty factor Q	780	600
Average power P, kW	28.5	11.8
Power flux from the neck surface, W/cm^2	24.3	2.7
Temperature jump at the neck due to peak power ΔT, K	34	1.3

Table 3.2: Electrical parameters of the focusing devices.

It is nesessary to note that the lenses are heated not only by a pulsed current, but by the beam energy deposition as well, which reaches the value of 9.8 J/cm^3/cycle at the neck region of lense L1 close to the internal surface. This result has been computed by program MARS'96 [7]. The Joule heating in the neck region is equal to 93 J/cm^3/cycle.

3.2 Cooling and Stress

The heating and stress produced by the current pulse of 320 kA in the inner conductor have been calculated by the finite element program HAST (Heating And STress, [8]) assuming the current time dependence as mentioned above.

As the current pulse duration $T \gg T_l$, where T_l is the period of lens resonant mechanical oscillations, the maximum stress of inner conductor due to magnetic pressure is defined by the static stress at a peak current. For the lenses L1 and L3 the lowest resonant frequencies are defined by longitudinal oscillations and equal to 6.845 kHz and 2.77 kHz respectively [9].

3.2.1 Lenses Cooling

The evolution of lens L1 temperature as a function of time for various heat transfer coefficients (HTC) from the lens surface is shown in Figure 3.1. One can see that the cooling system should provide the heat transfer coefficient of at least 6000 W/(m^2·K). The distribution of the maximum temperature along the lens for HTC = 7000 W/(m^2·K) is shown in Figure 3.2. As for the lens L3, our estimations show that HTC = 600 W/(m^2·K) is sufficient to cool its neck.

3.2.2 Stress

The inner conductor stresses due to the pulsed current have been calculated under the following boundary conditions:

- the ends of lenses assembly are rigidly clamped;
- the connecting flanges may move longitudinally;
- there is no longitudinal movements at the symmetry plane of lenses assembly.

The distributions of axial (σ_t) and circumferential (σ_φ) stresses in the lens L1 at room temperature produced by the current of 320 kA are shown in Figure 3.3. As the radial stress is very small, it is not shown. The largest stress at the neck is determined by (σ_t–σ_φ) = 45 N/mm^2. The lens is stretched at the neck region and compressed near flange. The point σ_t=0 corresponds to the place of welding.

The distributions of σ_t and σ_φ stresses for various instants of time after the steady state are represented in Figure 3.4.

Before the current pulse (Temp.=T_{min}, I=0), the stress is defined only by a temperature stress and is rather small, ~8 N/mm^2 (Figure 3.4a). At the peak current (T_{min} < Temp. < T_{max}, I = 320 kA), the maximum stress is determined by the longitudinal stress σ_t near the connecting flanges and equal to 34.6 N/mm^2 (Figure 3.4b). After the current pulse (Temp. = T_{max}), the maximum compression stress occures at the neck and equal to 49 N/mm^2 (Figure 3.4c). Such value of a stress corresponds to the dynamic fatigue stress limit of (6–7)×10^7 cycles [2],[9] (extrapolated value).

The compression is dangerous because the lens stability may be lost. The estimations show that the reserve of stability is equal to 2.4.

Prior to construction a full analysis of the lens stresses will be done by ANSYS computer code [10]. Perhaps it will be nesessary to make the stretched prestress to compensate for the average temperature rise and to minimize the compression at the welding place.

3.3 Radiation Problems

The absorbed dose and dose rate at the lenses of the WBB focusing system have been calculated using the program MARS'96 [7] for 3.7×10^{20} protons on target per year.

The absorbed doses for lens L1 are $(1.5–2)\times10^{10}$ Gy/year (Gy = J/kg) at the neck and $(2–3)\times10^{9}$ Gy/year near the connecting and end flanges. These doses for lens L3 are: $(6–7)\times10^{8}$ Gy/year and 10^{8} Gy/year respectively. Very high absorbed doses near the flanges practically exclude the usage of an organic insulation. All electrical insulation of the lenses and strip–line should be made of machinable ceramic with a radiation resistance more than 10^{10} Gy for lens L1 (3 years of operation) and 10^{9} Gy for L3 (10 years of operation).

The expected residual dose rates at the external surface of outer conductor after one year of operation as a function of time are given in Figure 3.5. Very high residual radiation levels exclude any repairs of the failed focusing devices.

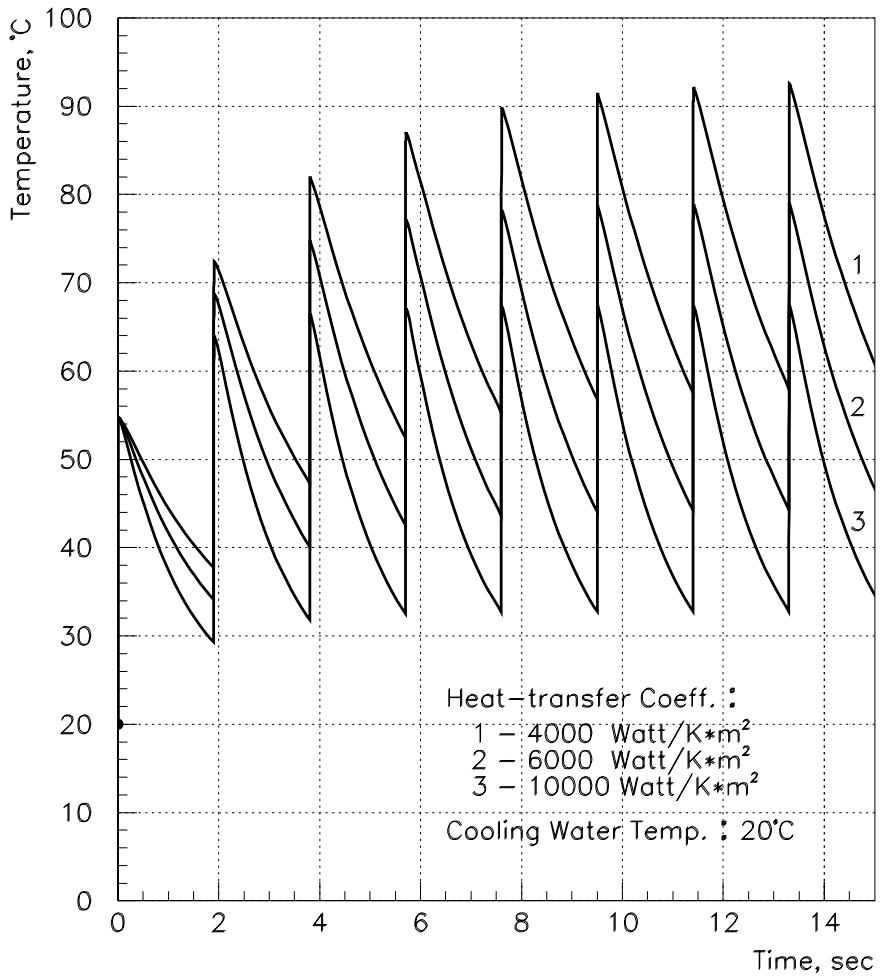

Figure 3.1: Temperature versus time in the neck region of the lens L1.

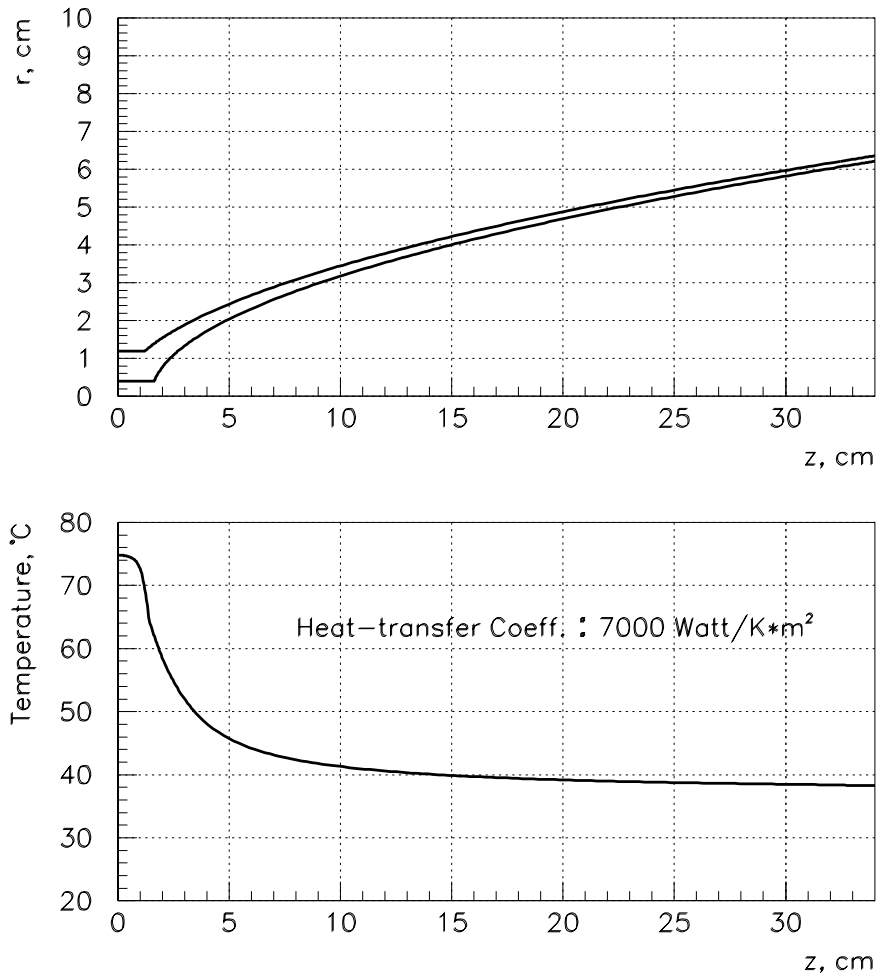

Figure 3.2: Maximum temperatures along the lens L1 in a steady state.

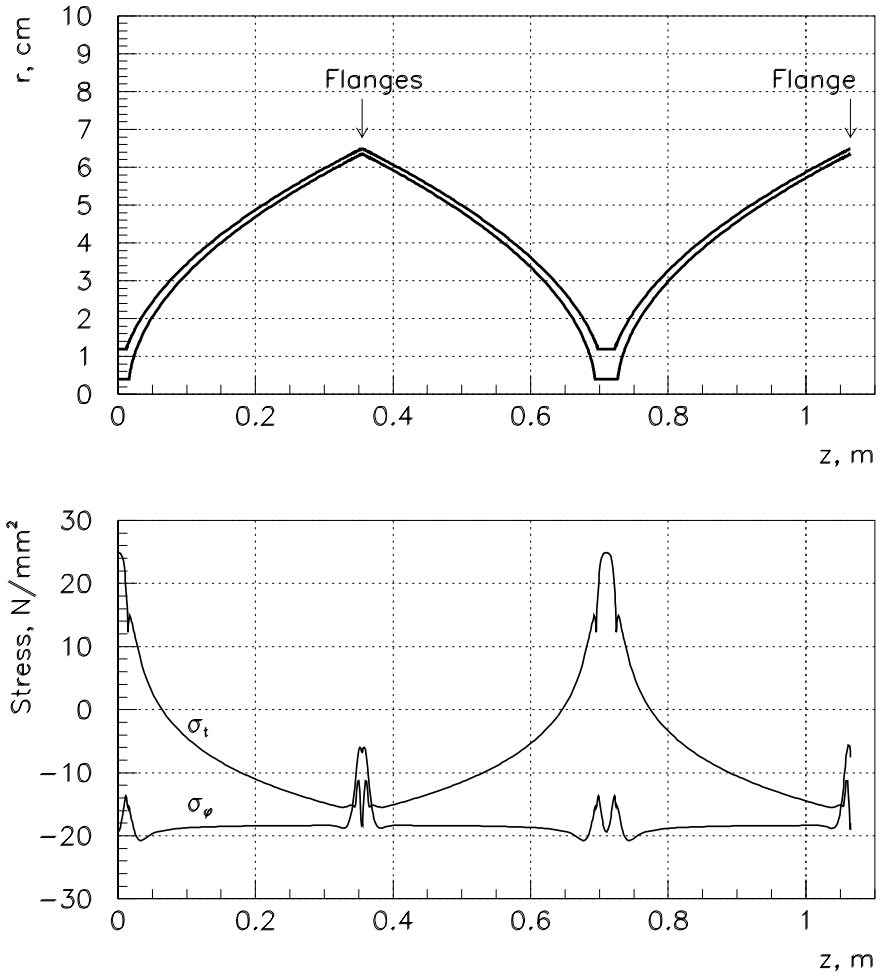

Figure 3.3: The axial (σ_t) and circumferential (σ_φ) stresses along the lens L1 produced by current 320 kA.

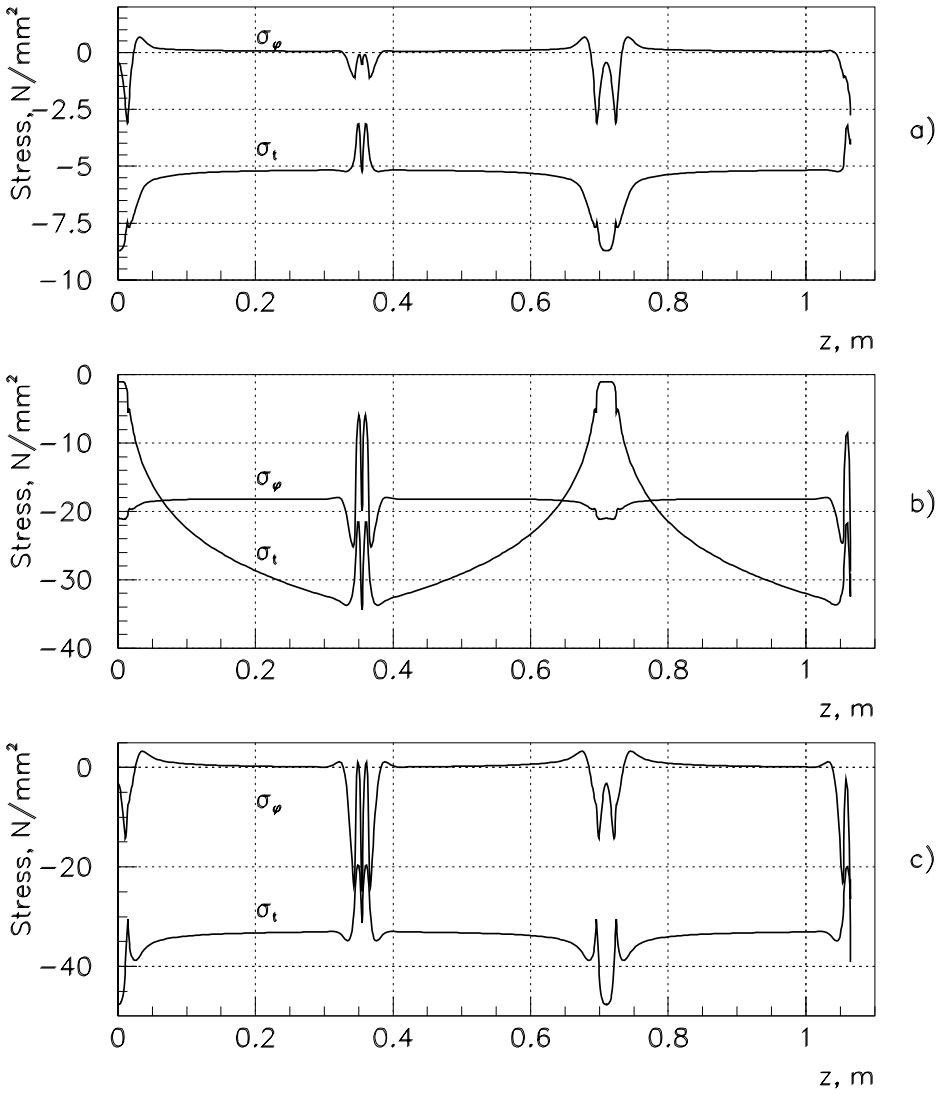

Figure 3.4: The axial (σ_t) and circumferential (σ_φ) stresses along the lens L1 before current load (a), at the peak of current pulse (b) and just after the pulse (c).

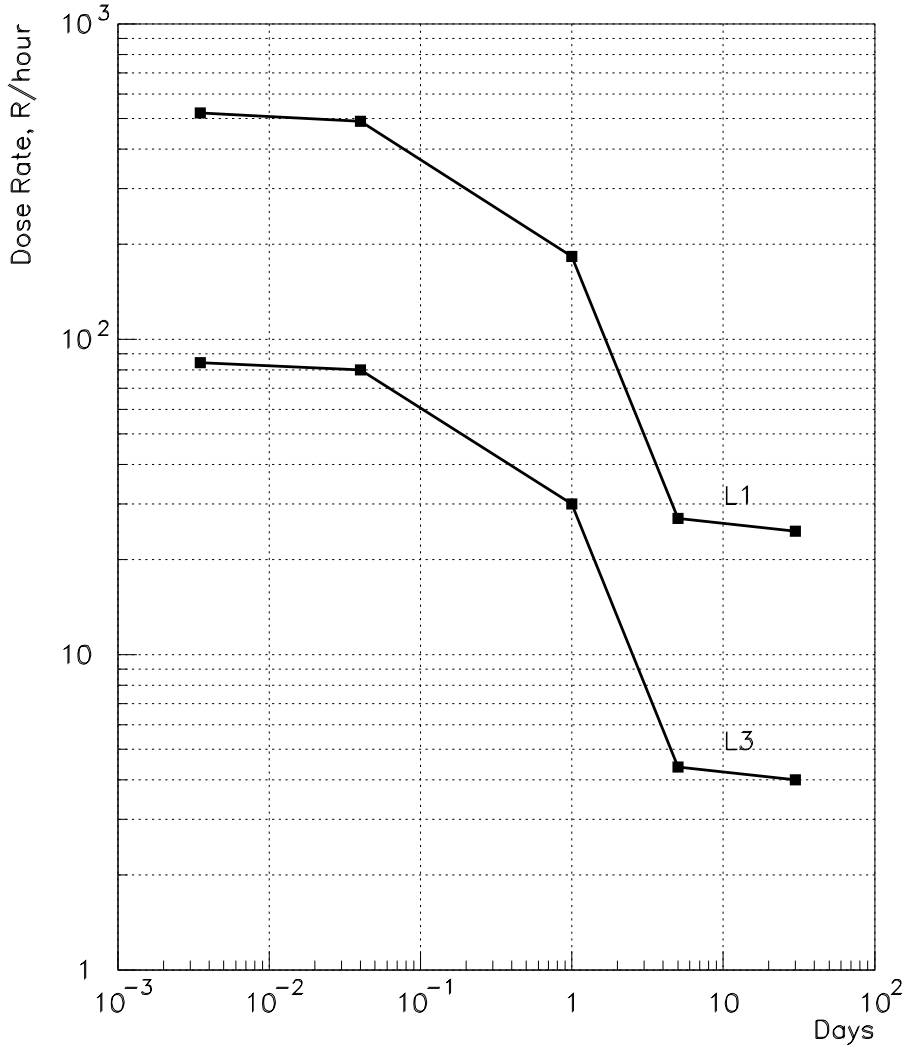

Figure 3.5: The expected residual dose rates at the outer conductors.

References

[1] N.Mokhov, FERMILAB–TM–628, Batavia, 1995.

[2] D.Baratov et al, IHEP Preprint 76-87, Serpukhov, 1987.

[3] NuMI Technical Design Report, NuMI-B-92, FERMILAB-TM-1946, Batavia, 1995.

[4] D.C.Carey and V.A.White, June 1975, PM0011.

[5] Ch.Iselin, CERN 74-17 Yellow Report, Geneva, 1974.

[6] D.Baranov et al, IHEP Preprint 78-136, Serpukhov, 1978.

[7] I.Azhgirey et al, Proc. XV Conference on Charged Particles Accelerators, p.74, Protvino, 1996.

[8] A.Abramov et al, IHEP Preprint 84-64, Serpukhov, 1984.

[9] V.Rykov, *Research and Design of the IHEP Neutrino Beam*, PhD, 1980.

[10] ANSYS 5.3 (1996), Swanson Analysis, Inc. Houston, PA.